SCIENTIFIC REPORTS

OPEN

On-chip coherent detection with quantum limited sensitivity

Vadim Kovalyuk[1,2], Simone Ferrari[2,3], Oliver Kahl[2,3], Alexander Semenov[1,4], Michael Shcherbatenko[1,4], Yury Lobanov[1,4], Roman Ozhegov[1], Alexander Korneev [1,4], Nataliya Kaurova[1], Boris Voronov[1], Wolfram Pernice[3] & Gregory Gol'tsman[1,5]

While single photon detectors provide superior intensity sensitivity, spectral resolution is usually lost after the detection event. Yet for applications in low signal infrared spectroscopy recovering information about the photon's frequency contributions is essential. Here we use highly efficient waveguide integrated superconducting single-photon detectors for on-chip coherent detection. In a single nanophotonic device, we demonstrate both single-photon counting with up to 86% on-chip detection efficiency, as well as heterodyne coherent detection with spectral resolution $f/\Delta f$ exceeding 10^{11}. By mixing a local oscillator with the single photon signal field, we observe frequency modulation at the intermediate frequency with ultra-low local oscillator power in the femto-Watt range. By optimizing the nanowire geometry and the working parameters of the detection scheme, we reach quantum-limited sensitivity. Our approach enables to realize matrix integrated heterodyne nanophotonic devices in the C-band wavelength range, for classical and quantum optics applications where single-photon counting as well as high spectral resolution are required simultaneously.

Nanophotonic circuits allow for realizing complex optical functionality on a chip and enable the assembly of functional devices with many optical components in a scalable fashion. Fast and efficient single-photon detectors represent one of the fundamental building blocks for the realization of on-chip quantum photonic circuits[1]. Superconducting nanowire single-photon detectors[2] (SNSPDs) are the most promising detection devices for telecommunication wavelengths. They combine high detection efficiency, low dark count rate, and high temporal resolution in a single device[3, 4] and have been successfully employed for classical and quantum optics applications[5]. In contrast to a more traditional detector geometry, in which light illuminates the nanowire surface under normal incidence, a travelling wave approach[6] allows drastically increased absorption efficiency due to evanescent coupling with a waveguided mode, resulting in a compact device which can be embedded within large-scale quantum photonic integrated circuits[7]. By adapting the length and the width of the nanowire, one can precisely control the detector absorption and the internal detection efficiency (IDE). This enables the realization of detectors with over 90% on-chip detection efficiency (η_{oc}) in the C-band[8]. To date, such hybrid superconducting-nanophotonic devices have been implemented on a variety of material platforms[9], including silicon on insulator (SOI), silicon nitride (Si_3N_4), gallium arsenide (GaAs) and polycrystalline diamond. The latest success of the traveling wave approach is associated with the detection of non-classical light on a chip[10, 11].

As threshold detectors, SNSPDs are not directly capable of giving information about the energy of the incident radiation. Integrated optics offers possible solutions, introducing additional elements such as arrayed waveguide gratings (AWG)[12], Mach-Zehnder interferometers[13], ring resonators[14], extended waveguides[15], diffraction gratings on planar waveguides[16] and photonic crystals[17]. However, all of these approaches offer only a small number of spectral channels, which results either in limited resolution or in a narrow spectral range.

An alternative way of determining the spectrum of unknown radiation is to use coherent detection[18]. With this technique, the detector absorbs radiation from two different sources (signal S and local oscillator LO) which are frequency-shifted relatively to each other. The response signal is a difference (intermediate) frequency (IF), corresponding to the beating frequency of the two fields. Knowing the LO frequency and measuring the IF allows to determine the frequency and phase of the unknown signal S.

[1]Department of Physics, Moscow State Pedagogical University, Moscow, 119992, Russia. [2]Institute of Nanotechnology, Karlsruhe Institute of Technology, Karlsruhe, 76132, Germany. [3]Institute of Physics, University of Münster, Münster, 48149, Germany. [4]Moscow Institute of Physics and Technology, Moscow, 141700, Russia. [5]National Research University Higher School of Economics, Moscow, 101000, Russia. Vadim Kovalyuk, Simone Ferrari and Oliver Kahl contributed equally to this work. Correspondence and requests for materials should be addressed to G.G. (email: ggoltsman@hse.ru)
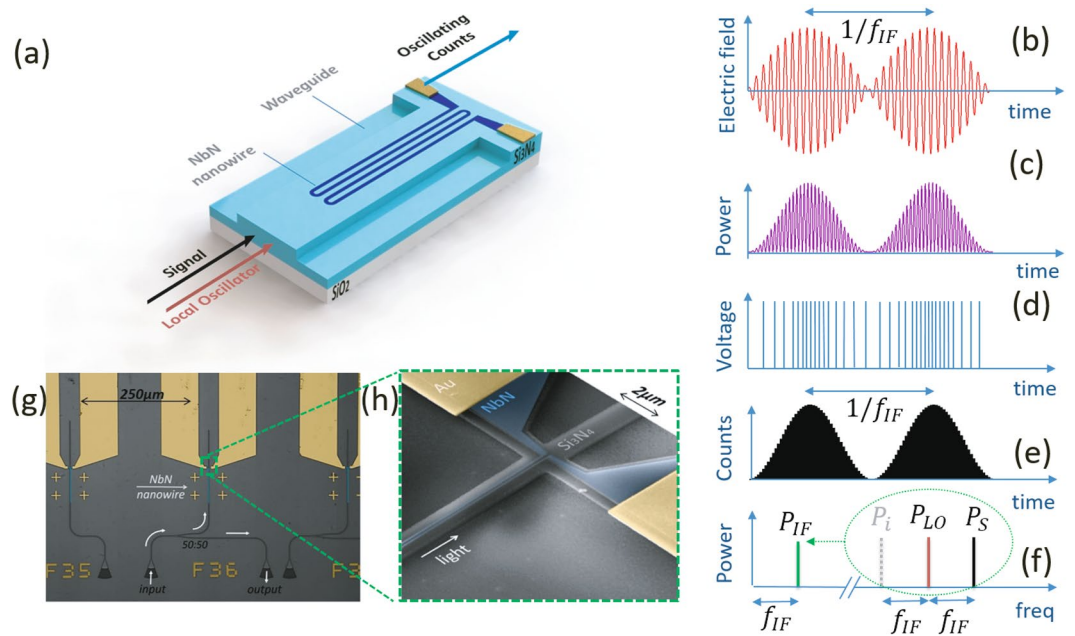
Figure 1. Operation principle of a SNSPD as a coherent detector and layout. (**a**) Schematic view of the SNSPD in coherent detection mode, in which two EM waves with slightly different frequencies (f_{LO}, f_S) are sent to the SNSPD. (**b**) Time domain beating of the EM-field generated overlapping LO and S fields, with slightly different frequencies. (**c**) Power oscillation in time at an intermediate frequency $f_{IF} = |f_{LO} - f_S|$. (**d**) Schematic representation of the detection pulses frequency modulation in presence of beating, which reproduces the optical power amplitude modulation. (**e**) Schematic view of the counts histogram vs time. By measuring the frequency of the counts oscillations f_{IF} and knowing the f_{LO}, one can determine the frequency of the unknown signal $f_S = |f_{LO} - f_{IF}|$. (**f**) Representation of the coherent detection in the frequency domain. The intermediate frequency is transferred from the IR range to a lower frequency. In addition to the signal and LO, the image channel contributes noise to P_{IF}. (**g**) False color optical micrograph of the nanophotonic devices. Each device consists of two focusing grating couplers, nanophotonic waveguides with a 50:50 Y-splitter, where one branch reaches a NbN nanowire connected to Au contact pads. (**h**) False color SEM image of a typical NbN nanowire atop a nanophotonic waveguide.

While analog detectors are normally used for coherent detection, recently, the use of a Geiger-mode operated InGaAs avalanche photodiode (APD) array for heterodyne detection at 1064 nm wavelength has been demonstrated in a single-photon counting regime[19, 20]. This approach allows to combine the detection of photons as well as heterodyne mixing and is of interest for Doppler shift detection of specular and diffused targets during LADAR investigation. Furthermore, using photon counters in the coherent detection allows to reduce LO power by more than 9 orders of magnitude from milli- to picowatts level. Potential of SNSPDs for coherent detection at telecommunication wavelength was introduced by Shcherbatenko et al.[21], where he demonstrated that a single pixel SNSPD is capable of taking over the entire functionality of an APD array, with LO power required of the order of a few pW and providing IF bandwidth up to 140 MHz. However, due to limited detection efficiency and nonscalability, the application of stand-alone SNSPDs for coherent detection is substantially limited.

Combining this technique and the superior sensitivity of SNSPDs on an integrated platform with high η_{oc} allows us to carry out on-chip heterodyne detection with high spectral resolution. We employ waveguide-integrated SNSPDs for on-chip coherent detection and demonstrate quantum limited sensitivity with a chip-based device. Our approach provides advantages not only for Doppler shift detection[19, 20] and weak signal frequency modulation[22], but also for integrated quantum optics technologies in the context of correlation and spectral characterization of on-chip narrowband single-photon sources[23, 24].

Results

The adopted coherent detection scheme requires two radiation sources, a signal (S) and a local oscillator (LO), with slightly different frequencies f_{LO}, f_S (Fig. 1a). The superposition of the two waves generates a beating signal with an amplitude which rises when the two signals are in phase and falls when in anti-phase (Fig. 1b). The beating power, defined as $P_{IF} = 2\sqrt{P_S P_{LO}} \cos(2\pi f_{IF} t + \varphi)$, oscillates at an intermediate frequency given by the difference of the two lasing frequencies: $f_{IF} = f_{LO} - f_S$ (Fig. 1c). As a consequence of this beating mode also the photon flux (Φ_{ph}), and therefore, the count rate (CR) from the detector oscillates at the same frequency f_{IF} (Fig. 1d,e). While the timestamp of each detection event is non-deterministic, the overall response probability is proportional to the incoming power in each time bin. In the presence of beating, the response probability is: $p(t) = \Phi_{ph}\eta_{oc}(1 + \alpha \cos(2\pi f_{IF} t + \varphi))$, where α is the modulation depth $\alpha = 2\sqrt{P_S P_{LO}}/(P_S + P_{LO})$. Knowing the LO frequency and measuring the intermediate frequency, it is then possible to determine the frequency of the unknown signal $f_S = |f_{LO} - f_{IF}|$ as well is its amplitude $P_S \propto P_{IF}^2/P_{LO}$.
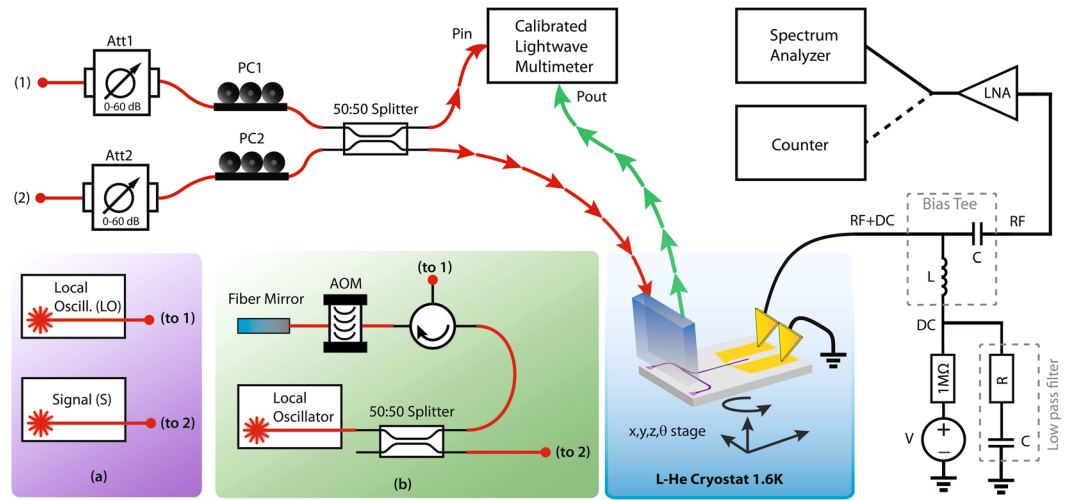
Figure 2. Experimental setups. Schematic view of the experimental setup for the single photon counting and the heterodyne mixing measurement. The nanophotonic device is mounted inside a liquid helium cryostat at a temperature of 1.6 K with optical access (red and green lines and arrows) and electrical access (black lines). (**a**) Coherent detection configuration in which two lasers are connected to points 1 and 2 in the basic scheme. (**b**) Single laser configuration for coherent detection, which allows us to use one laser source as LO and the signal. The generated laser light is divided in two by a 50:50 splitter. One branch of the splitter is directly routed to the mixing setup, while the second one is shifted by ≈ 400 MHz by the mean of an AOM.

Two different methods can be adopted to investigate the signal with a SNSPD in coherent detection mode. A first approach consists in registering the arrival time of the detection pulses in a pulse counter. The intermediate frequency is then $f_{IF} = 1/T_{beat}$, where T_{beat} is the period of the beating (Fig. 1e). A second approach consists in spectrally resolving the detection pulses train using a spectrum analyzer (SA), which converts the signal into the frequency domain providing power spectral density (PSD) of the signal (Fig. 1f). In practice, the integration time is determined by the desired frequency resolution and the frequency range in which the measurement is made. The stability of the LO determines the maximum frequency resolution, and the detector conversion bandwidth determines the frequency window in which measurements are usually made. In turn, the accumulation efficiency (signal-to-noise ratio) is proportional to the detection efficiency of the detector and limited by the detector and system noise. In order to increase the signal-to-noise ratio (SNR), sequences of the data accumulation steps could be repeated providing an averaged result, with the increase of the total measurement time. For this reason, efficient, low-noise and broadband detectors are desirable.

Device design. Color-enhanced optical and SEM pictures of the fabricated nanophotonic circuit are shown in Fig. 1g,h. The device structure includes two focusing grating couplers (FGC), a 50:50 Y-splitter and a nominal 4 nm thick NbN nanowire on top of the silicon nitride rib waveguide. For our experiment, we use SNSPDs with the same nanowire width (80 nm), but different length and shape. In particular, we use a W - shaped nanowire (WSN), 240 μm long, represented in Fig. 1a, and a U – shaped nanowire (USN) 140 μm long, depicted in Fig. 1h. The FGCs are used to inject light into a single mode nanophotonic waveguide and are also used for the collection of the transmitted light from the chip. The period and the fill factor of the FGCs are optimized for transmission at 1550 nm wavelength at liquid helium temperatures. The 50:50 Y-splitter is employed to route equal shares of the light to the SNSPD and to a second FGC, which serves as a reference to determine the photon flux reaching the detector.

Single-photon counting. The experimental setup for the characterization of the waveguide integrated single-photon counter is depicted schematically in Fig. 2. A calibrated photon flux is generated from a tunable laser source and attenuated by a calibrated optical attenuator Att_1 (see Supplementary Materials, S1). A polarization controller PC_1 is used to adjust the polarization of the fiber mode which is coupled onto the input FGC. The injected power P_{in} is monitored by a 50:50 beam splitter and an optical power meter. With the same instrument, the output power P_{out} from the calibration coupler has also been monitored. The measurements are performed according to a standard procedure[8], which main feature is the ability to determine the photon flux reaching the detector (see Methods for details).

The absorption of single photons by the superconducting NbN nanowire leads to a temporal breakdown of the superconducting state and generation of electrical voltage pulses[3, 4], which, after amplification, are registered by a counter. In Fig. 3a we show the dependence of the count rate (CR) of the WSN detector at different values of Φ_{ph}, as well as the corresponding dark count rate on the bias current I_b. For all curves the CR shows a pronounced plateau. This is indicative of high quality nanowires and implies that the internal detection efficiency saturates. We achieved a maximum efficiency value of $\eta_{oc} = 86 \pm 8\%$ for the WSN and $68\% \pm 7\%$ for USN setting an input photon flux at the detector of $\Phi_{ph} \leq 10^6$. We attribute the difference in the detection efficiency for the two detectors to an imporved absorption efficiency for the W-shaped geometry detector. For higher values of Φ_{ph} be observe a
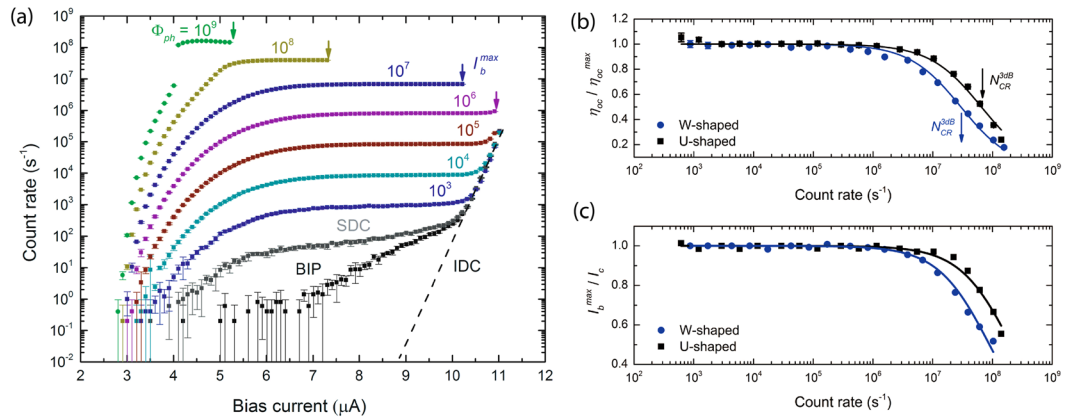
Figure 3. Measurement of the single-photon detector (SNSPD) performance. (**a**) Count rate of the W-shaped nanowire vs bias current, at different levels of optical power at 1550 nm wavelength. The photon flux is shown above each curve and marked by individual colors. The count rate when the laser is turned off but connected to an optical fiber at a room temperature is marked by SDC. The count rate with a closed metal cup is marked as BIP. The intrinsic dark counts marked as IDC (**b**) Dependence of the normalized on-chip detection efficiency (η_{oc}) on count rate. The black squares correspond to the measured data for U-shaped nanowire, while the blue dots for W-shaped nanowire. The fitted values are represented with solid lines and the arrows indicate the count rate N_{CR}^{3dB} at which $\eta_{oc}(N_{CR}^{3dB}) = \eta_{oc}^{max}/2$. (**c**) Normalized maximum current vs count rate. The black squares represent the measured dependence for U-shaped detector, while the blue dots for the W-shaped detector. The fitted values are represented with solid lines.

significant reduction of the η_{oc} (Fig. 3b). With increasing the photon flux reaching the nanowire, the number of photons impinging the detector during its dead time rises and hence the counting rate significantly decreases. The N_{CR}^{3dB} value at which the efficiency drops twice is indicated by the arrows in Fig. 3c and corresponds to a value of 3×10^7 and 6.8×10^7 counts per second for the WSN and USN, respectively. This different behavior can be attributed to the different value of the kinetic inductance L_k of the detectors, which is, by definition, directly proportional to the length of nanowire and inversely proportional to its width[25].

The same holds for the maximum value of the bias current I_b^{max} (Fig. 3c). In order to explain this behavior, which has been previously observed by Kerman *et al.*[26], we have to analyze the properties of the bias circuit in detail. A large number of clicks leads to charging of the capacitor in the bias tee (Fig. 2), introducing an additional bias voltage, in parallel to the main one. The average voltage value depends on the number of counts, on the shape and amplitude of the pulse from SNSPD. Extra current added to the current source leads to an increase of the supercurrent, which translate to a premature suppression of the superconductivity. At low count rates, the influence of the additionally charged capacitor is small, but becomes sufficiently large at count rates greater than 10^7 ph/s. This leads to the appearance of artifacts in dependence of count rate versus the bias current (see Supplementary Materials, S2), as well as to the need to reduce the bias current of the detector at high CR, and simultaneously reducing the detection efficiency in turn. This relationship allows us to select the optimal bias current conditions for coherent detection.

In addition to the intrinsic dark counts of the detector (IDC) (Fig. 3a), an additional noise contribution results from background induced photons (BIP), generated in the sample chamber from the 300 K parts of the cryostat insert, as well as by hot parts of the optical fiber[27]. The measurement of BIP has been performed with the fiber input closed by a metal cup. The dark count rate of the whole system, indicated as system dark counts SDC, has been performed without sealing the optical fiber input at the room temperature stage, which leads to an enhanced probability of detecting stray light. Improving the optical shielding of the detectors, as well as using a filter system[27] can significantly reduce SDC in the future down to IDC.

The timing characteristics of the detectors in use, i.e. the nanoseconds decay time (τ_D) and picoseconds jitter (τ_J) for the WSN, are determined as $\tau_D = 10 \pm 1$ ns and $\tau_J = 56 \pm 3$ ps and $\tau_D = 3$ ns ± 0.3 ns and $\tau_J = 60 \pm 3$ ps for the USN, respectively. The higher decay time for the WSN detectors can be again attributed to the higher kinetic inductance[25].

Despite the fact that the demonstrated on-chip detection efficiency is quite high (up to 86%), the system detection efficiency (SDE) is limited by the efficiency of the grating coupler $\eta_{SDE} = 0.86 \times 0.15 = 0.13$. For applications where higher SDE is required, the design of the FGC can be optimized[28] or replaced with alternative designs[29].

Coherent heterodyne detection with a single laser source.

To investigate the SNSPD as a coherent detector the emitted light from tunable laser source is divided into two parts using a 50:50 fiber beam splitter (Fig. 2). The first part acts as the LO, while the second part, routed twice through an acousto-optic modulator (AOM) to relatively shift its frequency to the initial carrier frequency of a constant value of $f_{IF} \approx 400$ MHz, acts as a signal S (Fig. 2b). Both light inputs from the LO and S are attenuated (Att$_1$, Att$_2$), routed through a polarization controller (PC$_1$, PC$_2$) and combined at the fiber optics beam splitter. A fiber array is used to conduct the light to
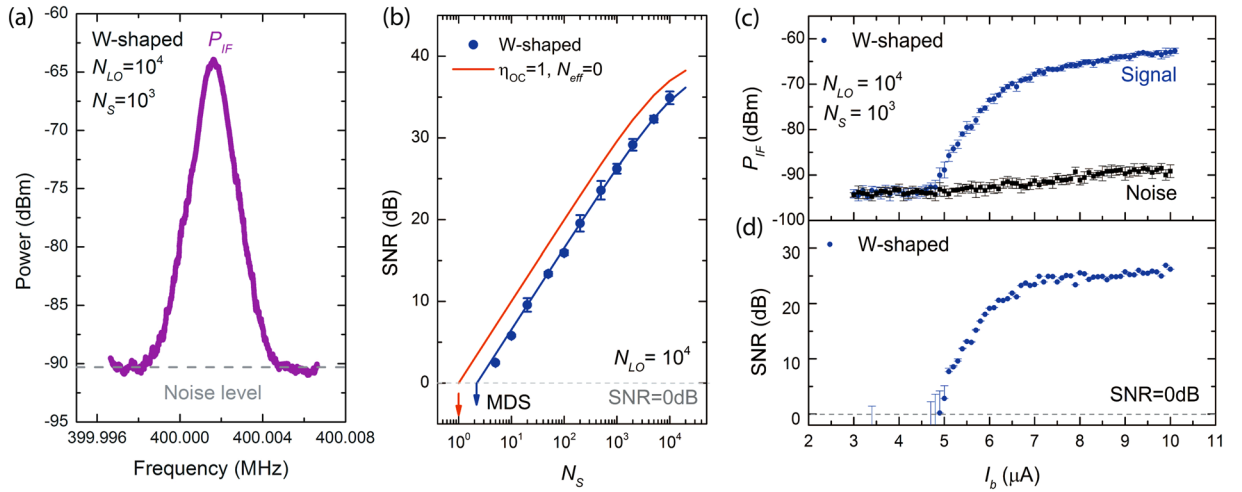
Figure 4. Measurement of the SNSPD performance as coherent detector. (**a**) Measured power vs frequency in the frequency range of $f_{IF} \pm 5$ kHz. (**b**) Measured SNR vs different signal N_S at fixed $N_{LO} = 10^4$ (blue dots). The red line indicates the simulated curve for an ideal shot-noise limited photodetector. The arrows indicate the N_S when SNR $= 0$ dB. (**c**) IF power for signal and noise vs bias current. (**d**) Extrapolated SNR vs bias current.

the nanophotonic devices, placed on a motorized stage (AttoCube Systems) in a cryostat at 1.6 K temperature (see Methods for details).

To analyze the intermediate frequency signal we used a spectrum analyzer (Rohde & Schwarz ZVL6). This method allows us to directly visualize the spectrum of the SNSPD detection pulses and evaluate the IF signal as well as all the contributions from the different noise sources. The voltage trace (pulses from SNSPD) is Fourier-transformed by the spectrum analyzer, and the square of the modulus of the Fourier-transform is represented as power (see Supplementary materials, S3).

The IF spectrum, obtained as a Fourier transform of the pulses train by the SA, includes (1) electrical noise of the system, (2) the power spectrum of a single pulse proportional to the total incident power ($P_{LO} + P_S$), and (3) the coherent signal due to the LO and S field beating, at which detection, we are interested on.

In a first step of the measurement protocol we select the desired resolution bandwidth (RBW) of the SA. By varying the RBW and measuring the IF power at $f_{IF} = 400.016$ MHz, we observed that the IF power does not significantly depend on the RBW down to 1 kHz. This indicates that the signal width at the IF is narrower. The signal amplitude is not cut out significantly for RBW ≥ 1 kHz (see Supplementary Materials, S4) and allows us to achieve high spectral resolution equal to $f/\Delta f \approx 193.5$ THz/1 kHz $\approx 1.935 \times 10^{11}$. The IF power of the WSN output for a RBW $= 1$ kHz is depicted in Fig. 4a. The spectrum shows a clear signal P_{IF} at the beat frequency $f_{IF} = 400.016$ MHz as well as the noise level (P_{noise}) (gray dashed line). The noise contribution mainly arises from two sources: the amplifier noise, and the power noise pulses generated by the detector (SDC and counts from LO, S).

The signal-to-noise ratio for the IF power detected by the SA can be defined as (see Supplementary Materials, S3):

$$SNR = \eta_{OC} m^2 \frac{N_S N_{LO}}{N_S + N_{LO} + N_{SDC} + N_{eff}} \equiv \eta_{OC} SNR_1,$$

(1)

where m^2 is the mixing efficiency[19, 20]. This value indicates how well the electromagnetic fields of the LO and the S overlap in the single-mode waveguide with the detector placed atop of it. For our analysis we assume $m^2 = 1$. N_S, N_{LO}, N_{SDC}, N_{eff} are the average numbers of photons collected in the time interval $t = 1/$RBW respectively from S, LO, system dark counts (including intrinsic dark counts, room stray light as well as background induced photons) and the effective electronics noise at IF. The total integration time in the frequency range of $f_{IF} \pm 5$ kHz, including 10 points with accumulation time $t = 1/$RBW is equal to $t_{total} = 10 \times 1$ ms $= 10$ ms. This mode can be used in applications when a quick response is needed. In our case, when a greater accuracy were preferred at the expense of time, the total integration time was 20 sec (Fig. 4a). The additional internal approximation by 32001 points, performed by the SA, meanwhile, does not affect the total accumulation time.

Experimentally the SNR can be determined as:

$$SNR = (P_{IF} - P_{noise})/P_{noise},$$

(2)

where P_{IF} and P_{noise} are the power of IF signal and noise respectively, measured by SA. In order to find the best operating condition, we first measured the dependence of P_{IF} versus I_b at fixed value of $\Phi_{LO} = 10^7$ ph/s. This photon flux corresponds to an average number of photons per integration time $N_{LO} = \Phi_{LO}/$RBW $= 10^4$ (Fig. 4c). In Fig. 4d we show the measured dependence of SNR vs I_b. The SNR increases with increasing I_b and shows the same plateau behavior as the on-chip detection efficiency of the detector, presented in Fig. 3a. The two quantities are
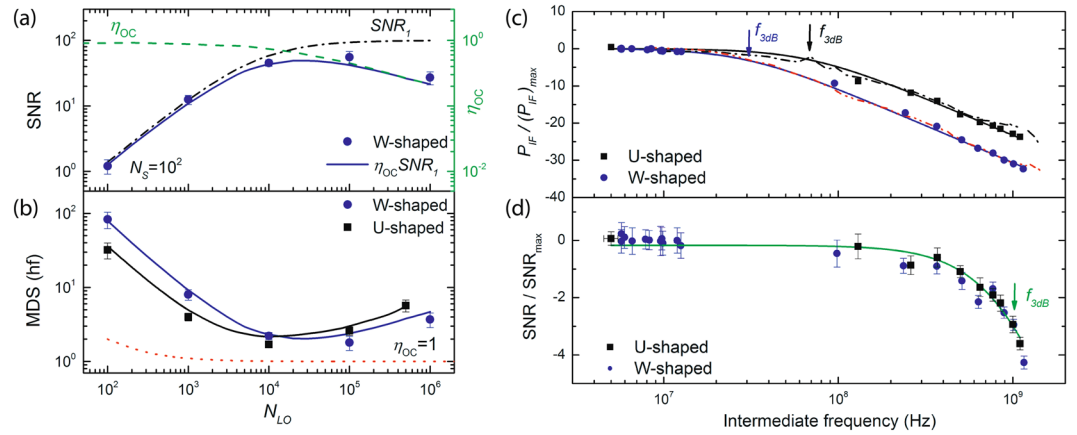
Figure 5. Measurement of the SNSPD performance as coherent detector. Blue dots correspond to the W-shaped nanowire and black squares to U-shaped nanowire. (**a**) Measured SNR vs N_{LO} at a constant signal $N_S = 10^2$. The green dashed line shows the measured dependence of η_{oc} (N_{LO}) and the black dash-dotted line represents the calculated SNR_1 with extracted data of N_{eff}. The blue solid line is the result of multiplication of η_{oc} (N_{LO}) and SNR_1 (**b**) Minimum detectable signal (MDS) in terms of single photons vs N_{LO}. The red dotted line shows the MDS for ideal shot noise limited detector (**c**) Measured IF bandwidth for both types of detectors. The dash-dotted lines show the Fast Fourier transform of a pulse detector. The fitted values are represented with solid lines and the arrows indicate the IF frequency f_{3dB} at which power decreases in two times. (**d**) Noise bandwidth vs f_{IF}. The fitted values are represented with the green solid line and the arrows indicate the IF frequency f_{3dB} at which SNR decreases in two times.

indeed correlated: at higher bias currents, the detection efficiency increases and consequently also the power at the intermediate frequency is also increased.

Keeping I_b constant at the corresponding maximum value of P_{IF} and setting a constant photon flux of the local oscillator N_{LO}, we determined the dependence of the SNR on the N_S. The experimental results and the fit to equation 1 are shown in Fig. 4b. When N_S, N_{SDC}, N_{eff} are small enough such that $N_{LO} \gg N_S + N_{SDC} + N_{eff}$, equation (1) reduces to SNR = $\eta_{OC} N_S$. The SNR depends linearly on N_S and starts to saturate when $N_S \approx N_{LO}$. If $N_S = N_{LO}$ and N_{SDC}, $N_{eff} \approx 0$, then is reduced by half: SNR = $\eta_{OC} N_S/2$. The same graph shows the calculated dependence of the SNR(N_S) for an ideal shot-noise limited mixer with $\eta_{OC} = 1$, $m^2 = 1$, $N_{SDC} = 0$, $N_{eff} = 0$. The arrows indicate the minimum detectable signal (MDS) for both cases, when the SNR = 0 dB. This corresponds to the condition $P_{IF} = 2 \times P_{noise}$, for the equation 2.

The same procedure has been applied for different N_{LO}. Figure 5a shows the dependence of the SNR(N_{LO}) at a fixed $N_S = 10^2$ for W-shaped detector. For small values of N_{LO} the relationship is linear, while it saturates and even decreases at larger values. The growth of the SNR with increasing N_{LO} can be associated with the overcoming of the effective noise of the electronics N_{eff}, while the drop can be associated with a reducing detection efficiency with increasing photon flux. According to the experimentally measured dependence of the PSD vs an incident photon flux, we have estimated the value of the effective noise N_{eff} for both types of nanowires at measured IF frequency 400.016 MHz (Supplementary Materials, S5). We found $N_{eff} = 7 \times 10^3$ for W-shaped and $N_{eff} = 2.6 \times 10^4$ for U-shaped detectors at the same RBW = 1 kHz.

The detectable signal reaches its minimum at values $N_{LO} \approx 10^4$–10^5 for both types of the detectors. The minima of the MDS is about 1.8–2.3 times the photon energy and close to MDS = 1 for the shot-noise limited mixer (Fig. 5b).

Coherent heterodyne detection with two laser source and IF bandwidth measurement. The same experimental setup which we used for characterizing the device sensitivity can be re-adapted for heterodyne detection using two lasers sources instead of one[18] (Fig. 2a). We employ two different lasers, one for generating the S signal at 1550.000 nm and a second for the LO at 1550.001 nm, corresponding to an initial frequency shift of ≈125 MHz. The photon flux was kept constant at $\Phi_S = 10^7$ ph/s and $\Phi_{LO} = 10^8$ ph/s. As previously asserted, mixing the signal of two different laser sources limits the IF frequency stability and therefore the measurements were carried out at RBW = 1 MHz in this case.

The measured P_{IF} versus f_{IF} is shown in Fig. 5c. The upper frequency limit of the conversion bandwidth of the mixer is defined as the cut-off frequency (f_{3dB}), corresponding to a decrease in IF signal power $P_{IF}(f_{IF} = 0)/P_{IF}(f_{3dB}) = 2$ and has been derived by fitting the intermediate frequency power spectra using the formula $P_{IF} = P_{IF}(f_{IF} = 0) - 10 \log_{10}(1 + (f_{IF}/f_{3dB})^2)$. The obtained conversion bandwidth for W-shaped detector was 29 ± 3 MHz, and for the U-shaped detector 68 ± 7 MHz. These values correspond to the N_{CR}^{3dB} at which the detector efficiency drops by a factor of two (Fig. 5c).

In addition to the conversion bandwidth we determined the noise bandwidth, defined as the intermediate frequency value at which the SNR is reduced by 3 dB, shown in Fig. 5d. With respect to the conversion bandwidth, the noise bandwidth does not depend on the detector length and reaches an upper frequency limit of 1040 ± 95 MHz. We associate the measured data with the amplifier bandwidth, while the theoretical prediction[21]

6

shows a jitter limited noise bandwidth equal to about $f_{jitter}^{3dB} = 2 \ln 2/\tau_J \approx 7.35$ GHz for the detectors. This prediction is encouraging for coherent detection with IF bandwidth for various applications, with the use of wide-bandwidth low noise cold amplifiers in the future.

Discussion

The calculated dependence of the minimum detectable signal on the local oscillator power N_{LO} for an ideal shot noise limited photodetector (red dash-dotted line), with unity detection efficiency as well as in complete absence of noise, is reported in Fig. 5b. When the LO power is much higher than the signal ($N_{LO} \gg N_S$), the incident signal integrated over the resolution bandwidth corresponding to the MDS equals hf and is independent of the LO power. This value increases to $2 \times hf$ for $N_{LO} = N_S$. However, we observed a dependence that differs from the ideal one (Fig. 5b). This can be explained considering the detector recovery time and noise contribution. At high photon flux, the detector does not have time to recover the original superconducting state, and η_{OC} is significantly reduced. This leads to a decrease of the SNR and an increase of the MDS, respectively. A reduction of the η_{OC} determines a practical upper limit to the LO power which can be used at the highest detection performance. Increasing the speed of the detector enables not only to increase the dynamic range for the LO power, but also to increase the conversion bandwidth (Fig. 5c). This can be done by reducing the length of the detector without compromising absorption and the IDE by embedding the detector inside a cavity[30], as well as through the optimization of the geometric parameters of the waveguide. On the other side, the LO power lower limit depends on the presence of additional noise in the system. Since the dark counts of the SNSPD are very small (for example, at $I_b < 10\,\mu A$, SDC/RBW < 1, see Fig. 2), the main noise contribution is the noise introduced by the experimental setup, especially the amplifiers at high frequencies (N_{eff}), which can be estimated by the power spectral density (Supplementary Materials, S5). Knowing N_{eff}, the SNR_1 can be then extracted (see equation 1) and by multiplying SNR_1 (Φ_{LO}) and η_{OC} (Φ_{LO}) we found a good agreement with the observed dependence of the SNR (N_{LO}) and MDS (N_{LO}).

Concerning the improvement of the detection procedure, we showed that the spectrum of the SNSPD pulse adds a noise contribution P_{noise} to the P_{IF}. The output power from the photon-counter includes the detector pulse itself (see Supplementary Materials, S3). Hence, by replacing an exponentially decaying pulse with a delta-function pulse, one could diminish the output noise related to the pulse spectrum. This can be done by registering the detection pulse arrival time points with a counter and performing the Fourier transform of this signal. Although this approach will not lead to an increase in the detector speed, which is determined mainly by the kinetic inductance[25], the IF bandwidth will not repeat the exponential pulse spectrum (Fig. 5c) and will be determined by the system noise, in analogy to the SNR bandwidth (Fig. 5d). Wide IF bandwidth is especially useful when operating devices without calibration, as well as for minimizing the influence of the N_{eff} at high frequencies (Supplementary Materials, S5).

Also, an advantageous spectrum analysis of wide-band signals can be carried out by combinational use of integrated-optics based wavelength dividers[12–17] allowing for partitioning the signal into discriminated spectrum-channels and fine spectrum analysis by the proposed heterodyne technique set up at each of the channels.

The coherent detection method demonstrated in this paper could also be successfully accomplished with SNSPDs implemented on a variety of material platforms[9] as well as other types of single-photon detectors, such as the transition edge sensors (TES)[31, 32] or commercially available free-running APDs[33, 34]. As a matter of fact, successful integration of a TES detector on an optical waveguide has already been demonstrated. Compared to SNSPDs, TES operation requires sub-kelvin temperatures with increased equipment costs. Concerning free-running APDs, considerable dark count rates (up to 6 kHz)[33] and afterpulsing probability (>5%)[34] limit the achievable MDS. In addition, integration on chip has not been demonstrated yet with APDs. Significant dead time (at a level of 0.1–100 μs) for TES and APDs leads to increased signal acquisition times, while lower timing resolution (>100 ps) decreases the achievable f_{jitter}^{3dB} bandwidth. In contrast, SNSPDs provide high on-chip detection efficiency, a low dark count rate, and high temporal resolution in a single device which makes them attractive for coherent detection on chip.

In conclusion, we have demonstrated heterodyne mixing with single-photon counting detector embedded in a travelling wave geometry approach, where the NbN nanowire is evanescently coupled to a waveguided mode field. We demonstrated single-photon counting with η_{oc} up to 86% and a coherent mixing with a spectral resolution ($f/\Delta f$) greater than 10^{11} at telecom wavelengths, operated close to the shot-noise limit. We further experimentally showed heterodyne detection at ultra-low local oscillator power (10^5–10^9 ph/s) and an extremely weak signal photon flux of the incident test signal (4×10^3–10^9 ph/s). A clear dependence between the conversion bandwidth and the nanowire geometry has been observed. In particular, shorter wires (U-shaped) showed greater throughput than longer (W-shaped) and can be used for coherent detection applications where narrow-line observations are required in a wide band. Lastly we commented on possible ways to further improve the performance of these detectors, that can be adopted for coherent detection in both classical and quantum optics.

Methods

Device fabrication.   The integrated hybrid architecture including waveguides and superconducting nanowire detectors (SNSPDs) is realized on commercially available silicon wafers Si (350–400 μm) with a thermal silicon oxide of SiO_2 (2600 nm) and silicon nitride Si_3N_4 (450 nm) grown on top. After cleaning the surface of the substrate we deposit an ultra-thin niobium nitride (NbN) film with a nominal thickness of 4 nm ± 0.5 nm. The deposition is made by a reactive magnetron sputtering in Argon and Nitrogen atmosphere. We reached a maximum critical temperature $T_c = 9.5$ K for films deposited at a substrate temperature $T_S = 800\,°C$ with partial pressures of Argon and Nitrogen of 6×10^{-3} and 2.5×10^{-4} mbar, respectively. The sheet resistance of the deposited NbN film

measured at room temperature is 620 Ohms/sq. After the superconducting NbN film deposition, nanophotonic devices are fabricated using three e-beam lithography steps. In the first step contact pads and alignment marks in a positive e-beam polymethyl methacrylate (PMMA) resist are defined. Then, by e-beam physical vapor deposition (ePVD) we deposit 5 nm of chromium (Cr) as an adhesion layer and 150 nm of gold (Au) and finalize the contact pads and the alignment marks by lift-off in acetone. In the second step, NbN nanowires are realized using HSQ resist and CF_4 reactive ion etching. The final step consists in patterning rib-waveguides into ma-N 2403 resist by e-beam lithography and obtaining the final device by dry etching the Si_3N_4 layer by RIE in CHF_3 plasma. Residual ma-N 2403 resist is then removed by an additional O_2 plasma cleaning step. In our case, the variation in thickness of the NbN superconductor film, as well as the quality of electron beam lithography affect the device yield the most. For this reason, we usually fabricate arrays of devices with slightly different parameters. Over a 2×2 cm sample we obtain device yield at a level of about 70%.

Measurement setup (single photon counting). To generate a calibrated photon flux we used a tunable laser source (New Focus TLB 6600) attenuated by an optical attenuator Att_1 (HP 8156A). A polarization controller PC_1 (Thorlabs FPC032) is used to adjust the polarization of the fiber mode which is coupled onto the input FGC. The injected power P_{in} is monitored by a 50:50 beam splitter and a calibrated Lightwave multimeter (HP 8163A). With the same instrument, the output power P_{out} from the calibration coupler has also been monitored. The photon flux reaching the detector can be written as $\Phi_{det} = (P_{in}/hf) \times S \times C \times WT_2$. Where S is the splitting ratio of the on-chip 50:50 Y-splitter, C is the coupling efficiency, WT_2 waveguide transmission of the arm leading to the nanowire. The coupling efficiency is determined from the input and output powers as: $C = \sqrt{P_{out}/(P_{in} \times S \times WT_1)}$, where WT_1 refers to the waveguide transmission for the calibration arm. The electrical readout circuit is composed of a stable current source CS (Keithley 2400), Mini-Circuits Bias Tees (ZFBT-GW6+) to separate RF and DC components, an RC filter and two low noise amplifiers (Mini-Circuits ZFL-1000LN+). The absorption of single photons by the superconducting NbN nanowire leads to a temporal breakdown of the superconducting state and generation of electrical voltage pulses, which, after amplification, are registered by a 225 MHz counter (HP 53132A). The on-chip detection efficiency is then determined as $\eta_{oc} = (CR - SDE)/\Phi_{det}$, where CR is the count rate and SDC is the system dark count rate.

Measurement setup (heterodyne detection). For demonstration of the on-chip coherent detection we use tunable laser source (TLS Santec 510). The emitted light is divided into two parts using a 50:50 fiber beam splitter. The first part acts as the LO, while the second part, routed twice through an acousto-optic modulator (AOM Gooch&Housego fibre Q) to relatively shift its frequency to the initial carrier frequency of a constant value of $f_{IF} = 400.016$ MHz, acts as a signal S (Fig. 2b). Both light inputs from the LO and S are attenuated (Att_1, Att2), routed through a polarization controller (PC_1, PC_2) and combined at the fiber optics beam splitter. A fiber array is used to conduct the light to the nanophotonic devices, placed on a motorized stage (AttoCube Systems) in a cryostat at 1.6 K temperature. The calibration of the radiation power incident on the input of the nanophotonic devices P_{in} is performed separately for each channel by switching the attenuators Att_1 and Att_2 off separately and by measuring the output power under the two respective input conditions. We note that the same characterization could also have been performed with two different lasers, one as source and a second one as local oscillator. We opted, however, for a single source in order to minimize the contribution of the frequency fluctuation of the laser output that could limit the detection resolution bandwidth and the overall system sensitivity at f_{IF}. For the heterodyne detection with two laser source and IF bandwidth measurement, we replaced in the main scheme the AOM and mirror with a second tunable laser source (New Focus NF6427).

References

1. Silverstone, J. W., Bonneau, D., O'Brien, J. L. & Thompson, M. G. Silicon Quantum Photonics. *IEEE J. Sel. Top. Quantum Electron.* **22**, 390–402 (2016).
2. Gol'tsman, G. N. *et al.* Picosecond superconducting single-photon optical detector. *Appl. Phys. Lett.* **79**, 705–707 (2001).
3. Hadfield, R. H. Single-photon detectors for optical quantum information applications. *Nat. Photonics* **3**, 696–705 (2009).
4. Natarajan, C. M., Tanner, M. G. & Hadfield, R. H. Superconducting nanowire single-photon detectors: Physics and applications. *Supercond. Sci. Technol.* **25**, 63001 (2012).
5. Najafi, F. *et al.* Superconducting nanowire architectures for single photon detection in *Superconducting Devices in Quantum* Optics (eds Hadfield, R. H. & Göran, J.) 3–30 (Springer, 2016).
6. Sprengers, J. P. *et al.* Waveguide superconducting single-photon detectors for integrated quantum photonic circuits. *Appl. Phys. Lett.* **99**, 181110 (2011).
7. Dietrich, C. P., Fiore, A., Thompson, M., Kamp, M. & Höfling, S. GaAs integrated quantum photonics: Towards compact and multi-functional quantum photonic integrated circuits Christof. *Laser Photonics Rev* **10**, 870–894 (2016).
8. Pernice, W. H. P. *et al.* High-speed and high-efficiency travelling wave single-photon detectors embedded in nanophotonic circuits. *Nat. Commun.* **3**, 1325 (2012).
9. Bogdanov, S., Shalaginov, M. Y., Boltasseva, A. & Shalaev, V. M. Material platforms for integrated quantum photonics. *Opt. Mater. Express* **7**, 111–132 (2017).
10. Najafi, F. *et al.* On-chip detection of non-classical light by scalable integration of single-photon detectors. *Nat. Commun.* **6**, 5873 (2015).
11. Schuck, C. *et al.* Quantum interference in heterogeneous superconducting-photonic circuits on a silicon chip. *Nat. Commun.* **7**, 10352 (2016).
12. Nishi, H. *et al.* Monolithic integration of a silica AWG and Ge photodiodes on Si photonic platform for one-chip WDM receiver. *Opt. Express* **20**, 9312–9321 (2012).
13. Florjańczyk, M. *et al.* Multiaperture planar waveguide spectrometer formed by arrayed Mach-Zehnder interferometers. *Opt. Express* **15**, 18176–18189 (2007).
14. Dong, P. *et al.* Low power and compact reconfigurable multiplexing devices based on silicon microring resonators. *Opt. Express* **18**, 9852–9858 (2010).
15. Velasco, A. V. *et al.* High-resolution Fourier-transform spectrometer chip with microphotonic silicon spiral waveguides. *Opt. Lett.* **38**, 706–708 (2013).

16. Kyotoku, B., Chen, L. & Lipson, M. Sub-nm resolution cavity enhanced microspectrometer. *Opt. Express* **18**, 102–107 (2010).
17. Momeni, B., Hosseini, E. S., Askari, M., Soltani, M. & Adibi, A. Integrated photonic crystal spectrometers for sensing applications. *Opt. Commun.* **282**, 3168–3171 (2009).
18. Jacobs, S. F. Optical heterodyne (coherent) detection. *Am. J. Phys.* **56**, 235–245 (1988).
19. Luu, J. X. & Jiang, L. A. Saturation effects in heterodyne detection with Geiger-mode InGaAs avalanche photodiode detector arrays. *Appl. Opt.* **45**, 3798–3804 (2006).
20. Jiang, L. A. & Luu, J. X. Heterodyne detection with a weak local oscillator. *Appl. Opt.* **47**, 1486–1503 (2008).
21. Shcherbatenko, M. *et al.* Potential of a superconducting photon counter for heterodyne detection at the telecommunication wavelength. *Opt. Express* **24**, 30474–30484 (2016).
22. Howard, S. S., Straub, A., Horton, N. G., Kobat, D. & Xu, C. Frequency-multiplexed *in vivo* multiphoton phosphorescence lifetime microscopy. *Nat. Photonics* **7**, 33–37 (2013).
23. Xia, K. *et al.* All-optical preparation of coherent dark states of a single rare earth ion spin in a crystal. *Phys. Rev. Lett.* **115**, 93602 (2015).
24. Perrot, A. *et al.* Narrow optical homogeneous linewidths in rare earth doped nanocrystals. *Phys. Rev. Lett.* **111**, 203601 (2013).
25. Kerman, A. J. *et al.* Kinetic-inductance-limited reset time of superconducting nanowire photon counters. *Appl. Phys. Lett.* **88**, 111116 (2006).
26. Kerman, A. J., Rosenberg, D., Molnar, R. J. & Dauler, E. A. Readout of superconducting nanowire single-photon detectors at high count rates. *J. Appl. Phys.* **113**, 144511 (2013).
27. Smirnov, K., Vachtomin, Y., Divochiy, A., Antipov, A. & Goltsman, G. Dependence of dark count rates in superconducting single photon detectors on the filtering effect of standard single mode optical fibers. *Appl. Phys. Express* **8**, 22501 (2015).
28. Chen, X., Li, C., Fung, C. K. Y., Lo, S. M. G. & Tsang, H. K. Apodized waveguide grating couplers for efficient coupling to optical fibers. *IEEE Photonics Technol. Lett* **22**, 1156–1158 (2010).
29. McNab, S. J., Moll, N. & Vlasov, Y. A. Ultra-low loss photonic integrated circuit with membrane-type photonic crystal waveguides. *Opt. Express* **11**, 2927–2939 (2003).
30. Akhlaghi, M. K., Schelew, E. & Young, J. F. Waveguide integrated superconducting single-photon detectors implemented as near-perfect absorbers of coherent radiation. *Nat. Commun.* **6**, 8233 (2015).
31. Gerrits, T. *et al.* On-chip, photon-number-resolving, telecommunication-band detectors for scalable photonic information processing. *Phys. Rev. A* **84**, 60301 (2011).
32. Calkins, B. *et al.* High quantum-efficiency photon-number-resolving detector for photonic on-chip information processing. *Opt. Express* **21**, 22657–22670 (2013).
33. ID Quantique, ID220 NIR Free-Running SPAD (16/03/2017), http://www.idquantique.com/photon-counting/photon-counting-modules/id220/ (2017).
34. ID Quantique, ID230 NIR Best Dark Count Rate (16/03/2017), http://www.idquantique.com/photon-counting/photon-counting-modules/id230/ (2017).

Acknowledgements

Author Contributions

W.P., G.G., A.K., conceived the experiment. N.K., B.V., V.K. performed the thin film deposition and O.K. fabricated the detector devices. O.K. and S.F. implemented the measurement platform and O.K., S.F. and V.K. measured the circuits. M.S., Y.L., R.O. and A.S. produced a numerical data calculation and modeling. All authors analyzed the data and jointly wrote the manuscript.

Additional Information

Supplementary information accompanies this paper at doi:10.1038/s41598-017-05142-1

Competing Interests: The authors declare that they have no competing interests.

Publisher's note: Springer Nature remains neutral with regard to jurisdictional claims in published maps and institutional affiliations.